International Journal of Micro Air Vehicles

ORIGINAL RESEARCH ARTICLE

Open Access

https://doi.org/10.48130/mav-0026-0023

*International Journal of Micro Air Vehicles* **2026**, 18: e022

# Launch phase robustification of a gun-launched unmanned aerial vehicle for rapid reaction missions

Zian Wang[1], Guoliang Liu[2], Can Cui[1,2], Jianmiao Yi[2], Yiheng Liu[2] and Chao Xu[1,2*]

[1] *College of Control Science and Engineering, Zhejiang University, Hangzhou, Zhejiang 310027, China*
[2] *Huzhou Research Institute of Zhejiang University, Aerospace Intelligent Agent Research Center, Huzhou, Zhejiang 313000, China*
* Correspondence: cxu@zju.edu.cn (Xu C)

## Abstract

Gun-launched unmanned aerial vehicles (GL-UAVs) are novel aircraft designed for rapid-response tasks such as emergency rescue and forest and wildfire patrols. During launch, unavoidable operational factors lead to variable-geometry disturbances, intense launch overload, and motor counter-torque. Structural deformation arising from wing and empennage deployment reshapes the UAV's outline and aerodynamic characteristics, altering lift, drag, and control torque, and consequently causing response lag or overshoot in the control system. To address these uncertain dynamics, this paper presents a disturbance-rejection control scheme tailored for the launch phase: an angular-rate tracking active disturbance rejection control (ADRC) approach based on the extended state observer (ESO), which realizes real-time estimation and compensation of lumped disturbances and model uncertainties. Moreover, segmented throttle control is deployed to curb peak roll angular velocity induced by counter-torque when motors start up. Monte Carlo simulations and actual flight tests confirm the effectiveness of the proposed launch control algorithm and manual stability augmentation strategy.

**Keywords:** Gun-launched UAVs, Variable geometry, Active disturbance rejection control (ADRC), Extended state observer (ESO), Segmented throttle control, Flight test

**Citation:** Wang Z, Liu G, Cui C, Yi J, Liu Y, et al. 2026. Launch phase robustification of a gun-launched unmanned aerial vehicle for rapid reaction missions. *International Journal of Micro Air Vehicles* 18: e022 https://doi.org/10.48130/mav-0026-0023

# Introduction

## Motivation

Unmanned aerial vehicles (UAVs) play an increasingly important role in scenarios such as patrol prevention, video tracking, high-altitude positioning, vehicle tracking, and target identification[1–5], significantly enhancing social and security services[6–8]. However, small and medium UAVs are limited by size and weight and therefore typically take off via hand-launch or ejection, often using folded fixed wings for a high lift-to-drag ratio. A typical sequence is: the UAV is packaged inside the launcher, propelled out by high-pressure gas, after which the V-tails and wings deploy to achieve fixed-wing flight (Fig. 1).

In this sequence, the launch phase is the most dynamically severe and failure-prone stage of the whole mission chain: the high overload at the launch instant can exceed the sensor range; wall friction can induce post-exit autorotation; wing/tail deployment introduces abrupt aerodynamic and inertia changes; and the propulsion motor produces reaction torque at startup. These factors are superimposed within an extremely short time window, placing stringent demands on the real-time disturbance-rejection capability of the control system. Disturbance rejection and stabilization tailored to the launch phase are therefore key to the mission success rate of gun-launched UAVs and form the focus of this paper.

## Launch system

A gun/tube launch system typically comprises the launch tube, a high-pressure gas or gas-generator unit, in-tube guidance and restraint mechanisms, and a release mechanism. The launch timeline can be summarized as: (i) the high-pressure gas accelerates the folded UAV to the required muzzle velocity within an extremely short time (accompanied by high launch overload); (ii) the UAV exits the tube and the restraint is released; (iii) the V-tails and then the wings deploy; (iv) the propulsion motor is unlocked and started, establishing fixed-wing flight. This timeline corresponds one-to-one with the control-strategy time nodes see $T_0$–$T_4$ in section *Control strategy for the launch process*.

Designing the autopilot for such a variable-geometry vehicle requires handling the following problems:

• Initial launch dynamics: the sudden acceleration during catapult launch can exceed the sensor range, causing velocity errors that the algorithm must compensate for to stabilize the UAV quickly.

• Friction-induced rotation: friction between the UAV and the launcher wall can cause autorotation on exit, which must be corrected immediately for a stable, controlled trajectory.

• Wing and tail deployment: the dramatic aerodynamic changes from deployment introduce model disturbances affecting lift, drag, and stability.

• Propulsion-motor activation: motor startup exerts an undesirable reaction torque on attitude that the control system must counteract.

• Aerodynamic variability, center-of-gravity shift, high-speed control response, sensor calibration, and environmental factors must also be handled by robust control.

## Contribution

Both traditional and modern control approaches have been studied for variable-geometry platforms. Adaptive control, such as L1 adaptive control combined with dynamic inversion, has been applied to variable-sweep morphing aircraft to handle configuration-induced nonlinearities and maintain tracking performance over

© The Author(s)

https://doi.org/10.48130/mav-0026-0023



**Fig. 1** Flight experiment of the launch process of this paper.

a wide flight envelope[9]; $H_\infty$ control handles disturbance rejection and model uncertainty well and has been validated on UAVs[10,11]. Model-based methods such as gain scheduling are structurally complex with limited robustness, and their design tends to be empirical[12].

Besides the proposed scheme, nonlinear model predictive control (NMPC) is widely applied to control platforms with uncertainties. Although it can handle system constraints, NMPC involves massive online optimization calculations and obvious time delays, which cannot satisfy the fast response requirements during the launch phase of GL-UAVs. In comparison, active disturbance rejection control (ADRC) aggregates uncertain dynamics into a lumped total disturbance, which is estimated and compensated in real time by an extended state observer (ESO). ADRC delivers fast tracking and strong disturbance rejection, requires no precise system model, and boasts simple design and implementation[13–16]. Recently, the combination of hierarchical sliding mode control and control barrier functions has been applied to constrained attitude stabilization of underactuated systems.

Over the past 5 years, ADRC and its core components, the ESO and the $\mathrm{fal}(\cdot)$ function, have also evolved: the Hfal function improves ESO smoothness and reduces output chatter in noisy environments[17,18]; nested linear ESOs (LESO) improve disturbance-estimation accuracy without increasing bandwidth[17]; and adaptive ESOs (AESO) combine the merits of linear ESOs with adaptive techniques to extend to nonlinear systems[19].

Based on this comparison, this paper adopts a cascaded ADRC built around the ESO, because its combined advantages in robustness, disturbance rejection, fast response, model independence, and design simplicity best fit the engineering needs of the GL-UAV launch phase.

The main contributions of this work are as follows:

• Disturbance rejection for launch-phase transients: a cascaded ESO-based angular-rate stabilizer specifically handles abrupt aerodynamic and inertia changes during fold-to-deploy and the motor-startup reaction torque, markedly improving disturbance rejection over conventional algorithms.

• Segmented throttle control (novel engineering contribution): segmented slow acceleration suppresses motor-startup reaction torque, reducing the measured peak roll rate from 0.42 to 0.26 rad/s (about 38%) so the system meets the launch-success criteria.

• Clear and reproducible launch-success criteria: the subsection *Criteria for the successful launch process* gives quantitative criteria (e.g., roll rate converging to ± 0.05 rad/s within 1.5 s after full throttle), providing an objective, reproducible benchmark for similar gun-launched/catapult UAVs.

# Materials and methods

## Aircraft layout

In this paper, we introduce a small variable-geometry UAV characterized by a low-wing and V-tail configuration. As shown in Fig. 2, both the wings and V-tails can be folded. The wings fold below the fuselage, while the V-tails fold along the sides of the fuselage. The parameters of the UAV system are described using the following abbreviations: RI for rotational inertia, UN for undeployment, and DE for deployment.

• Weight (kg): 13
• Wing span (m): 0.2 (UN), 1.9 (DE)
• Reference area ($m^2$): 0.02 (UN), 0.22 (DE)
• Launch air pressure (MPa): 2.3 (UN), 2.3 (DE)
• RI of body $x_b$-axis (kg $m^2$): 0.0234 (UN), 0.299 (DE)
• RI of body $y_b$-axis (kg $m^2$): 1.103 (UN), 0.919 (DE)
• RI of body $z_b$-axis (kg $m^2$): 1.103 (UN), 1.189 (DE)

We define the body-fixed frame $x_b$, $y_b$, $z_b$ as shown in Fig. 2. The aerodynamic model is necessary to divide the wing into two parts: the unfolded fuselage part and the folded wing part. We first obtained clean aerodynamic forces and moments of the wing body part and then amended the unfolded fuselage part. The equation is

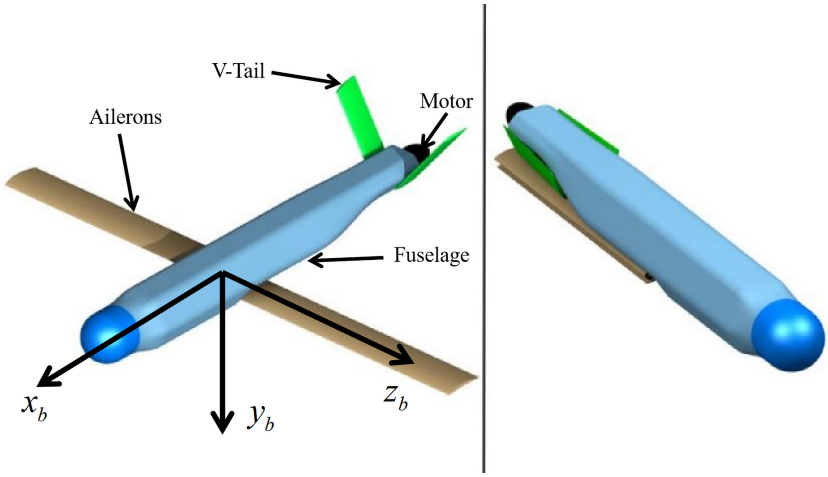



**Fig. 2** The layouts of small variable-geometry UAV: left side, wings unfolded; right side, wings folded.

$$\begin{cases} C_x = C_x(V,\alpha,\beta,\delta_e) \\ C_z = C_z(V,\alpha,\beta,\delta_e) \\ C_y = C_y(V,\alpha,\beta,\delta_a,\delta_r) \\ L = L(V,\alpha,\beta,\delta_a,\delta_r) \\ M = M(V,\alpha,\beta,\delta_e) \\ N = N(V,\alpha,\beta,\delta_a,\delta_r) \end{cases}. \tag{1}$$

Here, $\alpha$ and $\beta$ represent the aerodynamic angles, and $V$ denotes the airspeed. The symbols $C_x$, $C_y$, and $C_z$ correspond to the aerodynamic forces, while $L$, $M$, and $N$ denote the aerodynamic moments. The variables $\delta_a$, $\delta_e$, and $\delta_r$ are the virtual inputs for the aileron, elevator, and rudder, respectively.

The aerodynamic coefficients are obtained from Computational Fluid Dynamics (CFD) simulations and stored as interpolation (look-up) tables, which are evaluated online as functions of airspeed, angle of attack, sideslip angle, and control-surface deflections.

The roll, pitch, and yaw channels are represented by the virtual inputs $\delta_a$, $\delta_e$, and $\delta_r$, which are then mapped to physical surfaces by control allocation. For a V-tail, pitch and yaw are inherently coupled: symmetric deflection of the two V-tail surfaces produces a pitch moment while differential deflection produces a yaw moment, requiring decoupling through a mixing matrix. In the folded configuration, the tail and wings are not fully deployed, so surface effectiveness is much lower and inter-channel coupling is stronger than in the deployed configuration. Accordingly, the control law switches the surfaces participating in the loop across phases (see $T_2$–$T_4$ in section *Control strategy for the launch process*).

The nonlinear model contains forces, moments, kinematics, and navigation and can be organized as in[6,7].

The deformation dynamics of a projectile-launched transformable UAV are governed by a set of equations that describe the forces, moments, and motions involved during the transformation process. These equations include

**Aerodynamic forces and moments:**

$$\mathbf{F}_{\text{aero}} = \frac{1}{2}\rho V^2 S\, \mathbf{C}_F(\alpha,\beta,\delta_e,\delta_a,\delta_r), \tag{2}$$

$$\mathbf{T}_{\text{aero}} = \frac{1}{2}\rho V^2 S\, \mathbf{C}_M(\alpha,\beta,\delta_e,\delta_a,\delta_r), \tag{3}$$

where, $\rho$ is the air density, $V$ is the velocity, $S$ is the reference area, and $\mathbf{C}_F \in \mathbb{R}^{3\times1}$ and $\mathbf{C}_M \in \mathbb{R}^{3\times1}$ are the aerodynamic force and moment coefficients, which depend on the angle of attack ($\alpha$) and sideslip angle ($\beta$).

Control forces and moments are computed from $\delta_a$, $\delta_e$, and $\delta_r$, the dynamic pressure, and surface-effectiveness coefficients, and are distinguished from the passive aerodynamic moments.

**Rotational motion equations:**

$$\mathbf{I}\frac{d\boldsymbol{\omega}}{dt} + \boldsymbol{\omega}\times(\mathbf{I}\boldsymbol{\omega}) = \mathbf{T}_{\text{ext}}, \tag{4}$$

where, $\mathbf{I} \in \mathbb{R}^{3\times3}$ is the moment of inertia tensor, $\boldsymbol{\omega} \in \mathbb{R}^{3\times1}$ is the angular velocity vector, and $\mathbf{T}_{\text{ext}} \in \mathbb{R}^{3\times1}$ represents the external torques acting on the UAV.

The kinematic relationship between the pitch angle $\theta$ and the pitch angular rate $q$[1] is

$$\dot{\theta} = q\cos\phi - r\sin\phi, \tag{5}$$

where, $\phi$ is the roll angle and $r$ is the yaw angular rate.

It projects body-frame rates onto the inertial attitude rate and is the bridge between the outer attitude loop and the inner angular-rate loop in the cascade: the outer loop generates a rate command from the attitude error, and the inner loop tracks it.

**Translational motion equations:**

$$m\frac{d^2\mathbf{r}}{dt^2} = \mathbf{F}_{\text{ext}}, \tag{6}$$

where, $m$ is the mass of the UAV, $\mathbf{r} \in \mathbb{R}^{3\times1}$ is the position vector of the center of mass, and $\mathbf{F}_{\text{ext}} \in \mathbb{R}^{3\times1}$ represents the external forces acting on the UAV, such as thrust, drag, and gravity.

The translational motion equations are retained in the full dynamic model for two main reasons. First, flight velocity, angle of attack, and sideslip angle, which are essential for calculating aerodynamic coefficients in Eq. (6), are derived from translational states. Second, these equations are used to calculate launch overload and reproduce the ballistic trajectory during the gun-launch phase. Since the proposed controller only focuses on attitude and angular-rate regulation without velocity/position closed-loop control, translational dynamics do not appear in the control block diagram, but are still necessary for high-fidelity simulation.

**Deformation equations:**

$$\mathbf{M}\frac{d^2\mathbf{u}}{dt^2} + \mathbf{C}\frac{d\mathbf{u}}{dt} + \mathbf{K}\mathbf{u} = \mathbf{F}_{\text{int}}, \tag{7}$$

where, $\mathbf{u} \in \mathbb{R}^{3\times1}$ is the deformation vector, $\mathbf{M} \in \mathbb{R}^{3\times3}$ is the mass matrix, $\mathbf{C} \in \mathbb{R}^{3\times3}$ is the damping matrix, $\mathbf{K} \in \mathbb{R}^{3\times3}$ is the stiffness matrix, and $\mathbf{F}_{\text{int}} \in \mathbb{R}^{3\times1}$ represents the internal forces due to deformation.

$\mathbf{F}_{\text{int}}$ denotes the structural internal force caused by wing and tail deployment. It will introduce extra attitude disturbances and must be suppressed in controller design.

These equations must be solved simultaneously to accurately predict the UAV's behavior during launch, transformation, and subsequent flight. Advanced numerical methods and simulations are often employed to analyze these dynamics and ensure reliable performance.

## Control strategy for the launch process

Before launch, the wings and V-tails are folded and loaded into the launcher (Fig. 3). High-pressure gas first pushes the UAV out of the tube, after which the wings and V-tails deploy and the propulsion motor is activated. As shown in Fig. 4, the specific control strategy for the launch process is listed as follows:

• When the autopilot receives the launch command, high-pressure gas pushes the vehicle out of the tube; this instant is denoted as $T_0$. The in-tube propulsion rapidly accelerates the UAV to the required initial speed. The inertial measurement unit (IMU) continuously measures the $x_b$-axis acceleration, and if it exceeds 60 m/s² three times (the thrust required for launch), the launch is deemed successful and the propulsion motor is unlocked immediately.

• $T_1$: the IMU estimates the vehicle's velocity and angular rate; the velocity is determined by integration from the launch velocity.

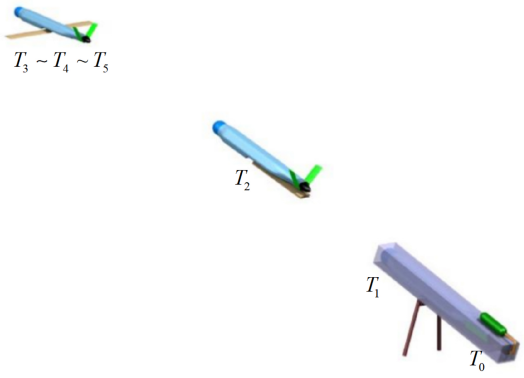



**Fig. 3** Animation of launch process.

https://doi.org/10.48130/mav-0026-0023

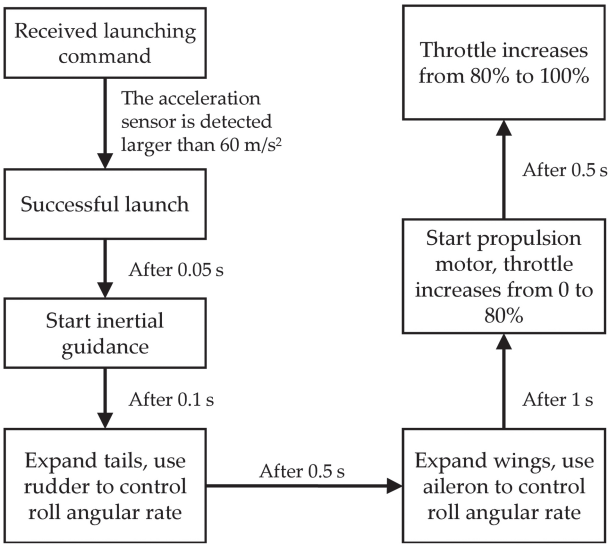



**Fig. 4** Control strategy for the launch process. High-pressure gas firstly pushes the UAV out of the launcher, and then the wings and V-tails deploy and the propulsion motor is activated.

• $T_2$: the V-tails deploy. The elevator maintains the pitch angle at 5° (launch angle), and the rudder suppresses roll by regulating the roll rate to 0°/s. Immediately after launch, the trajectory is approximately parabolic; to minimize longitudinal maneuvering, the pitch command is set to follow the tangent of the parabola.

• $T_3$: the wings deploy. The ailerons regulate the roll rate to 0°/s, while the elevator maintains the pitch angle at 5°.

• $T_4$: the propulsion motor is activated. To mitigate propeller reaction torque, a segmented slow-acceleration strategy is adopted: the throttle increases from 0% to 80% gradually, and then increases from 80% to 100% approximately 0.5 s later. After reaching 100%, the throttle is held for 4 s before entering the acceleration phase.

## Cascaded control design

A cascaded ADRC attitude controller is adopted to stabilize the launch process. The attitude dynamics are separated into a fast inner loop (angular rate) and a slow outer loop (attitude angle), and the control gains are tuned according to the timescale-separation principle. Given the actuator reconfiguration during launch, the virtual control inputs $q_c$ and $p_c$ are introduced as intermediaries to achieve the desired outputs. The complete control architecture is shown in Fig. 5.

The designed cascaded controller aims to stabilize UAV attitude and angular rate during launch, so independent velocity feedback control is not adopted. The translational motion model is reserved to describe force-moment coupling and support numerical verification, rather than participating in real-time control.

### *Cascaded longitudinal control*

The pitch angle rate command $\dot{\theta}_c$ is defined as

$$\dot{\theta}_c = k_\theta(\theta_c - \theta), \tag{8}$$

where, $k_\theta$ is the bandwidth of the outer-loop controller. Then, from Eq. (8), the pitch angular rate command $q_c$ is derived as

$$q_c = \frac{1}{\cos(\phi)}\dot{\theta}_c + r\sin(\phi) \quad . \tag{9}$$

Taking the derivative of both sides of Eq. (9), we obtain

$$\ddot{\theta} \approx \dot{q}\cos\phi + q\dot{\phi}\sin\phi - \dot{r}\sin\phi - r\dot{\phi}\cos\phi \quad . \tag{10}$$

By rotational dynamics,

$$\dot{q} = \frac{M - pr(I_x - I_z)}{I_y} \tag{11}$$

where, $p$ is the roll angular rate and $I_x$, $I_y$, and $I_z$ are the rotational inertias.

Combining Eqs (10) and (11), the dynamics can be written as

$$\ddot{\theta} = f_q + M_{\delta_e}\delta_e, \tag{12}$$

where, $M$ denotes the total pitch moment, $M_{\delta_e}$ is the pitch control efficiency, and $f_q$ is the lumped disturbance of the pitch angular rate loop, which can be organized as

$$f_q = -\dot{r}\sin\phi - r\dot{\phi}\cos\phi + q\dot{\phi}\sin\phi + \frac{M - (I_x - I_z)pr}{I_y}\cos\phi - M_{\delta_e}\delta_e \quad . \tag{13}$$

Define $y_q = \dot{\theta}$, $x_{1q} = \dot{\theta}$, and $x_{2q} = f_q$. Then Eq. (12) can be rewritten as

$$\begin{cases} \dot{x}_{1q} = x_{2q} + b_q\delta_e \ , \\ \dot{x}_{2q} = w \ , \\ y_q = x_{1q} \ , \end{cases} \tag{14}$$

where, $b_q = M_{\delta_e}$ is the control-efficiency-related parameter and $w$ is the derivative of the lumped disturbance.

To reduce the phase delay, a second-order nonlinear ESO is used in the pitch angular rate control loop:

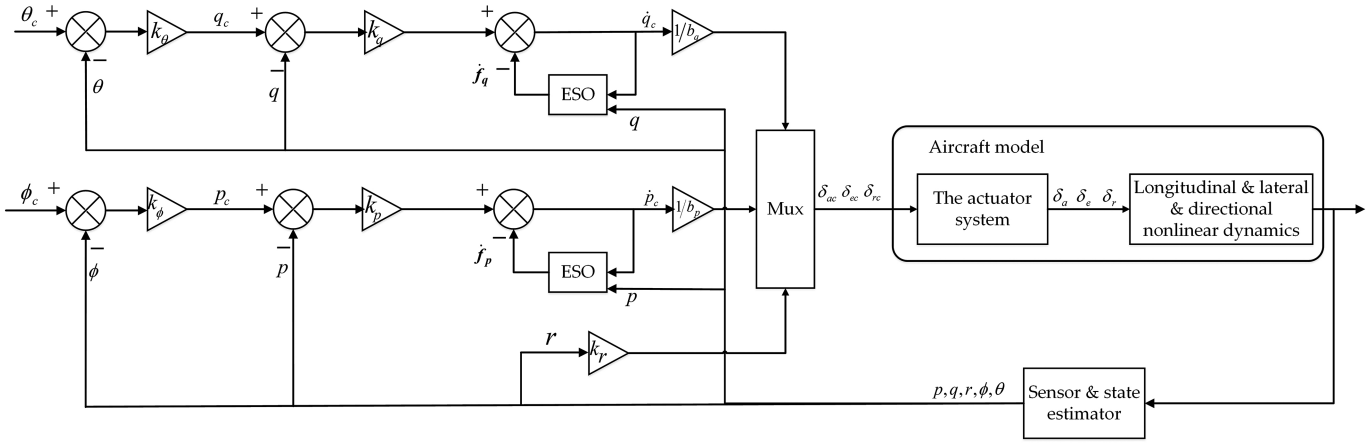



**Fig. 5** Complete control architecture. Pitch and roll cascaded ESO-based control schemes to handle the control stabilization.

$$\begin{cases} e_{1q} = z_{1q} - y_q, \\ \dot{z}_{1q} = z_{2q} + b_q u_q - \beta_{1q} e_{1q}, \\ \dot{z}_{2q} = -\beta_{2q}\,\mathrm{fal}(\mathrm{e}_{1q}, \alpha, \delta), \end{cases} \tag{15}$$

where, $z_{1q}$ and $z_{2q}$ are the estimations of the pitch angular rate and lumped disturbance, respectively, and $\beta_{1q}$ and $\beta_{2q}$ are the ESO parameters. The nonlinear function $\mathrm{fal}(\cdot)$ is defined as

$$\mathrm{fal}(e_{1q}, \alpha, \delta) = \begin{cases} \dfrac{e_{1q}}{\delta^{1-\alpha}}, & |e_{1q}| \leqslant \delta, \\ |e_{1q}|^{\alpha}\,\mathrm{sign}(e_{1q}), & |e_{1q}| > \delta. \end{cases} \tag{16}$$

where, the sign function is defined as

$$\mathrm{sign}(x) = \begin{cases} 1, & x > 0, \\ 0, & x = 0, \\ -1, & x < 0. \end{cases} \tag{17}$$

The observer parameters satisfy $\alpha \in [0, 1]$ and $\delta > 0$. By utilizing $\mathrm{sign}(\cdot)$, the $\mathrm{fal}(\cdot)$ function can also be written as

$$\begin{cases} s = \dfrac{\mathrm{sign}(e_q + \delta) - \mathrm{sign}(e_q - \delta)}{2}, \\ \mathrm{fal}(e_q, a, \delta) = \dfrac{e_q}{\delta^{1-a}} s + |e_q|^{a}\,\mathrm{sign}(e_q)(1 - s). \end{cases} \tag{18}$$

With a given parameter of $\mathrm{fal}(\cdot)$, the linear interval grows as $\delta$ increases. In particular, when $a = 1$, we have $\mathrm{fal}(e_q, 1, \delta) = e_q$. When $a = 0$, the function becomes

$$\mathrm{fal}(e_q, 0, \delta) = \begin{cases} \mathrm{sign}(e_q), & |e_q| > \delta, \\ \dfrac{e_q}{\delta}, & |e_q| \leqslant \delta. \end{cases} \tag{19}$$

In this case, $\mathrm{fal}(\cdot)$ is transformed into a saturation function.

Combining the nonlinear ESO in Eq. (14), the estimation error can be constructed as

$$\begin{cases} e_{2q} = z_{2q} - x_{2q}, \\ \dot{e}_{1q} = e_{2q} - \beta_{1q} e_{1q}, \\ \dot{e}_{2q} = -\beta_{2q}\,\mathrm{fal}(e_{1q}, \alpha, \delta) - w. \end{cases} \tag{20}$$

The pitch angular rate control law is

$$u_q = \frac{u_{0q} - z_{2q}}{b_q}, \tag{21}$$

where, $u_{0q}$ is the output of the proportional controller

$$u_{0q} = k_q(q_c - q), \tag{22}$$

where, $k_q$ represents the bandwidth of the pitch angular rate loop. From Eq. (12), the original plant can be tuned to a pure integrator plant, and the closed inner-loop transfer function can be reorganized as

$$\frac{\omega(s)}{\omega_c(s)} = \frac{k_q}{s + k_q}. \tag{23}$$

### *Cascaded lateral-directional control*

Similar to the pitch channel, the roll dynamics can be written as

$$\dot{p} = f_p + L_{\delta_a}\,\delta_a, \tag{24}$$

where, $f_p$ is the lumped disturbance of the angular rate loop, which can be organized as

$$f_p = \frac{(I_y - I_z)I_z}{I_x I_z} rq + \frac{I_z}{I_x I_z} L - L_{\delta_a}\,\delta_a, \tag{25}$$

where, $L_{\delta_a}$ is the roll control efficiency and $L$ denotes the roll moment induced by the rotor and aerodynamics. It can be summarized as follows:

• Significant changes happen in $I_x$ and aerodynamic moments from folding to deployment states.

• A relatively high gyroscopic moment is caused by the motor at its activation window.

The roll angular rate control law is

$$u_p = \frac{k_p(p_c - p) - z_{2p}}{b_p}, \tag{26}$$

where, $b_p = L_{\delta_a}$ is the control-efficiency-related parameter and $k_p$ is the bandwidth of the roll angular rate loop. The corresponding ESO is

$$\begin{cases} e_{1p} = z_{1p} - y_p, \\ \dot{z}_{1p} = z_{2p} + b_p u_p - \beta_{1p} e_{1p}, \\ \dot{z}_{2p} = -\beta_{2p}\,\mathrm{fal}(e_{1p}, \alpha, \delta). \end{cases} \tag{27}$$

The vehicle's deployable state shows a pronounced Dutch roll mode. To simplify the yaw channel control design, only damping stabilization is implemented. The damping control law can be organized as

$$u_r = k_r r. \tag{28}$$

The closed-loop stability analysis, including observability and controllability, can be referred to in Benyahia et al.[5].

### *Determination of ESO/fal(·) parameters and generalization*

The ESO gains $\beta_1$ and $\beta_2$ are tuned by bandwidth parameterization[17,18] from a single observer bandwidth $\omega_o$, i.e., $\beta_1 = 2\omega_o$ and $\beta_2 = \omega_o^2$, which reduces multi-parameter tuning to a single bandwidth choice. The observer bandwidth $\omega_o$ is chosen within the range 5–10, and is set to 5 in this work.

The $\mathrm{fal}(\cdot)$ parameters are set to $\alpha = 0.5$ and $\delta = 0.01$. Here, $\alpha = 0.5$ is a common compromise between disturbance rejection and smoothness, and $\delta = 0.01$ matches the measured angular-rate noise level of this platform.

Thanks to this parameterization, porting the proposed scheme to another gun-launched UAV only requires re-selecting $\omega_o$ and $\delta$ according to its angular-rate noise and actuator bandwidth; the tuning dimension is low, the rule is clear, and $\alpha$ can usually remain 0.5. Therefore, the method is transferable with light re-tuning rather than redesigning the control structure.

# Results

## Simulation parameters and model settings

### *Parameter settings for launch process simulation model*

The launch process is simulated by MATLAB/Simulink. Three artificial disturbances are introduced into the simulation:

• The spontaneous rotation caused by the friction between the UAV and the launcher's wall is simulated when the vehicle is launched out of the tube.

• The disturbance caused by the deployment of the wings is simulated. The V-tail is close to the fuselage, and the disturbance to the vehicle can be ignored.

• The torque caused by motor activation is also simulated.

The amplitudes and time histories of these roll-moment disturbances are not heuristic but are identified from measured flight data of the launch process, so that the simulated disturbances reproduce the magnitude and characteristics of the real launch environment. For the present vehicle, the equivalent roll-moment disturbances are on the order of a few N·m, which is consistent with the post-launch attitude excursions observed in the flight tests. This data-driven setting ensures that the conclusion that the proposed controller can cope with realistic disturbances is supported by representative disturbance levels rather than by artificially conservative ones.

https://doi.org/10.48130/mav-0026-0023

### *Disturbance simulation model and parameter settings of inner-loop control*

The trimming point is set at an airspeed of 36 m/s and an altitude of 50 m. The second-order systems with position and rate limitations are matched to the actuators. The characteristics of the actuators are: the aileron, elevator, and rudder have a natural frequency of 8 Hz, a damping ratio of 0.8, a position limitation ± 25°, and a position rate limitation ± 100°/s, as shown in Table 1. We design the ADRC controller abiding by the following control specifications:

- Level 1 flying qualities.
- Time-delay margin greater than 100 ms.
- Gain margin greater than 6 dB.
- The static error of the step response is within 0.05.

The ESO-related control parameters are shown in Table 2.

### *Relationship between control gains and stability margins*

Table 2 lists the inner-loop angular-rate gains ($k_q$, $k_p$) and the extended-state-observer (ESO) bandwidth $\omega_o$, while the outer attitude loops use $k_\theta$ and $k_\phi$. Because the ESO reduces each angular-rate channel to an approximate integrator, the inner-loop open-loop gain crossover frequency $\omega_c$ is set directly by $k_q$ and $k_p$, whereas the high-frequency phase lag is governed jointly by the actuator dynamics of Table 1 and the finite reconstruction bandwidth $\omega_o$. For margin analysis, these combined lags are represented by a reduced second-order model. The combined effect is equivalent to a pair of dominant large-inertia poles, which makes the high-frequency phase fall steeply and therefore sets an upper bound on how large $\omega_c$ and $\omega_o$ may be chosen before the stability margins collapse.

Sweeping the gain crossover frequency reveals a consistent trend. At low $\omega_c$, the gain margin (GM), phase margin (PM), and time-delay margin (TDM) are all generous, and the loop is highly tolerant of transport delay. As $\omega_c$ increases, the PM and GM decrease monotonically, and the loop becomes progressively less tolerant of transport delay; pushing the crossover well beyond the recommended band drives the PM toward the 45° limit and the GM toward the 6 dB threshold. Among the three margins, the TDM decays the most steeply with increasing crossover frequency, so for an embedded flight controller subject to communication and servo latency, the time-delay margin is the first specification to be approached. The same trade-off applies to the observer: increasing $\omega_o$ speeds up disturbance reconstruction but adds phase lag, so an excessively fast observer erodes PM and TDM in the same way.

To verify this relationship quantitatively, frequency-domain stability margins were computed over a sweep of the two bandwidth parameters, and the results are shown in Fig. 6. The left column fixes the observer bandwidth ($\omega_o$ = 20 rad/s) and sweeps the control crossover frequency $\omega_c$ from 1 to 10 rad/s; the right column fixes $\omega_c$ = 6 rad/s and sweeps the observer bandwidth $\omega_o$ from 10 to 60 rad/s. In every panel both PM and TDM decrease monotonically as the corresponding bandwidth increases, which confirms the qualitative trend above. For the control-gain sweep the PM stays above 45° across the entire 1–10 rad/s range while the TDM contracts from over 1 s to about 0.13 s; for the observer sweep the PM falls through the 45° line near $\omega_o \approx$ 40 rad/s, which establishes a practical ceiling on the observer bandwidth.

Table 3 summarizes the margins read from these sweeps at the design-relevant operating points. The adopted gains $k_q$ = 6 and $k_p$ = 10 place the angular-rate loops at $\omega_c \approx$ 6 rad/s, which lies near the center of the admissible window $\omega_c$ = 4–9 rad/s and yields PM = 68.5° and TDM = 214 ms, with GM ≥ 6 dB by design—comfortably satisfying the GM > 6 dB, TDM > 100 ms, and level 1 flying-qualities requirements. The adopted observer bandwidth $\omega_o$ = 20 rad/s sits well below the 40 rad/s ceiling, preserving the same margins. The outer-loop gains $k_\theta$ = 1.5 and $k_\phi$ = 2 are one order of magnitude below the inner-loop bandwidth, so by the time-scale separation established in section *Cascaded control design*, they do not erode the inner-loop margins.

These results give three porting rules for the present platform. First, the recommended operating band is $\omega_c$ = 4–9 rad/s, which guarantees PM > 45° and GM ≥ 6 dB. Second, if a faster response is required, the observer bandwidth $\omega_o$ should be raised in steps—using the additional phase lead to compensate for the roll-inertia lag—while keeping it below the 40 rad/s ceiling. Third, where transport delay is significant, $\omega_c$ should be lowered to prioritize the TDM. Taken together, the sweep in Fig. 6 and the margins in Table 3 close the chain from the Table 2 control gains, through the resulting stability margins, to the claimed level 1 flying qualities, thereby providing the analytical and simulation verification requested.

**Table 1.** Characteristics of the actuators.

| Actuator | Natural frequency (Hz) | Damping ratio | Position limitation (°) | Position rate limitation (°/s) |
|---|---|---|---|---|
| Aileron | 8 | 0.8 | ± 25 | ± 100 |
| Elevator | 8 | 0.8 | ± 25 | ± 100 |
| Rudder | 8 | 0.8 | ± 25 | ± 100 |

**Table 2.** ESO-related control parameters.

| Parameter | Value |
|---|---|
| ESO fal function, $\alpha$ | 0.5 |
| ESO fal function, $\delta$ | 0.01 |
| Pitch angular rate ESO gain, $\beta_{1q}$ | 20 |
| Pitch angular rate ESO gain, $\beta_{2q}$ | 100 |
| Roll angular rate ESO gain, $\beta_{1p}$ | 20 |
| Roll angular rate ESO gain, $\beta_{2p}$ | 100 |
| Bandwidth of pitch inner-loop, $k_q$ | 6 |
| Bandwidth of roll inner-loop, $k_p$ | 10 |
| Bandwidth of pitch outer-loop, $k_\theta$ | 1.5 |
| Bandwidth of roll outer-loop, $k_\phi$ | 2 |

## Key protection and control logic during launch

### *Protection logic for acceleration saturation during the launch process*

The acceleration during ejection is shown in Fig. 7. At the moment of ejection, the acceleration reaches 175 m/s$^2$, which exceeds the IMU's maximum range of 160 m/s$^2$. This data saturation results in inaccurate acceleration readings, leading to errors in velocity and position calculations, and consequently causing significant drift and error accumulation in the navigation solution. To address this issue, we disregard the IMU's acceleration data before launch and instead use the theoretically calculated launch velocity.

### *Identification of V-tail/wing deployment window based on acceleration fluctuation ($T_2$, $T_3$)*

Through the analysis of the acceleration data of the ejection tests, it is found that there will be two acceleration fluctuations during the launch process, which are caused by the expansion of the V-tail and the wing. Therefore, the exact deployment windows of the V-tail and the wing, namely $T_2$ and $T_3$, can be obtained. Based on the V-tail and wing deployment time, the elevator and aileron participation closed-loop stabilization control time can be determined.

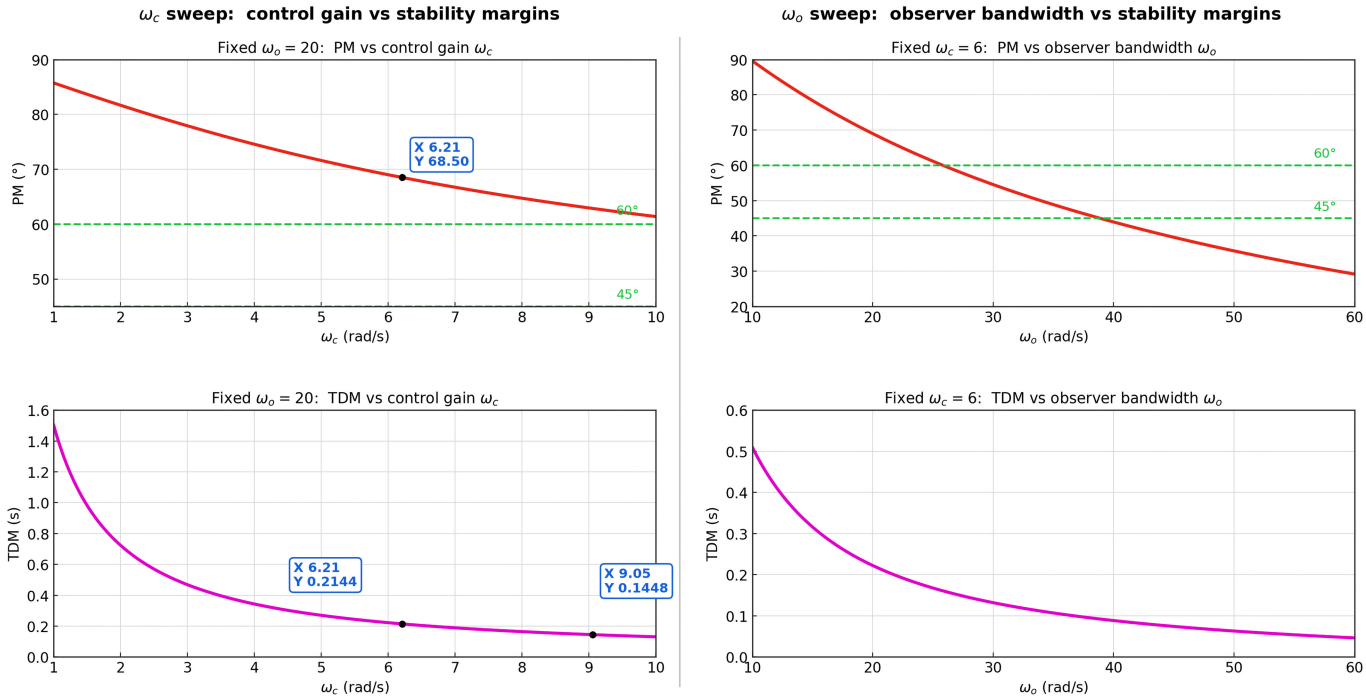



**Fig. 6** Simulation verification of stability margins. Left: control-gain sweep ($\omega_c$) at fixed $\omega_o$ = 20 rad/s. Right: observer-bandwidth sweep ($\omega_o$) at fixed $\omega_c$ = 6 rad/s. Dashed lines mark the 45° and 60° PM references.

**Table 3.** Stability margins at the design operating points (from the sweeps of Fig. 6).

| Operating point | GM (dB)* | PM | TDM (ms) | Level 1/margin spec |
|---|---|---|---|---|
| $\omega_c$ = 6, $\omega_o$ = 20 | ≥ 6 | 68.5° | 214 | Adopted design point—met |
| $\omega_o$ ≈ 40 rad/s | – | = 45° | ≈ 90 | Observer-bandwidth ceiling |
| $\omega_o$ > 40 rad/s | – | < 45° | < 90 | Over-fast observer: margins eroded |

* The gain margin (GM) at the adopted design point is specified by design to be ≥ 6 dB.

### *Segmented throttle control strategy (suppression of roll peak upon motor startup)*

To eliminate the sharp roll torque peak induced by a sudden full-speed start of the propulsion motor, a segmented throttle scheduling scheme is designed in this subsection. The motor output power is increased gradually in multiple staged increments rather than by a one-step maximum command. The step size and holding time of each throttle segment are matched with the structural unfolding sequence. This gentle power-up mode weakens the instantaneous asymmetric rolling moment, restrains the peak roll angular rate, and alleviates the regulation burden of the attitude control loop.

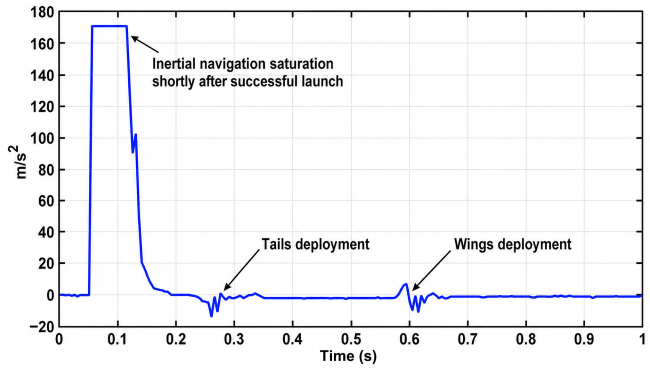



**Fig. 7** The evolution of acceleration vs time throughout the whole launch process.

## Simulation results of launch process stability

According to the previous launch data, it can be known:

The first disturbance is introduced 0.1 s after the ejection; the second disturbance is introduced 0.5 s after a successful launch; and the third disturbance is introduced 1.5 s after a successful launch. As shown in Fig. 8, the orange curve represents the roll angular rate, and the blue curve represents the pitch angular rate. It can be concluded that, after wing deployment, all actuators can normally participate in control, and the disturbances exerted at $T_2$ (V-tail deployment) and $T_3$ (wing deployment) are quickly suppressed. Two seconds after the propulsion motor starts, the vehicle's angular rates converge to 0 rad/s, and the attitude is stabilized, demonstrating that the ESO-based control method effectively enhances launch-phase stability.

But at $T_4$, the full rate of the propulsion motor leads to a relatively large roll angular rate peak. To reduce this undesired peak, we introduce a practical segmental throttle control strategy. The throttle whole acceleration process is divided into two stages:

- Increase the throttle from 0% to 80%, while maintaining the throttle steady at 80% for 0.5 s.
- Increase the throttle from 80% to 100%.

The time histories for the roll and pitch angular rate adopting the segmental throttle control strategy are shown in Fig. 9. It can be concluded that the peak value of roll angular rate decreases from 0.42 rad/s initially to 0.26 rad/s currently, which makes the vehicle attitude more stable and achieves the desired goal.

## Robustness verification: Monte Carlo simulation

### *Parameter perturbation settings (inertia, control coefficient, aerodynamic coefficient, thrust)*

To better verify the robustness and tracking performance under model parameter perturbations, Monte Carlo simulations are conducted. The related uncertainties are shown in Table 4.

https://doi.org/10.48130/mav-0026-0023

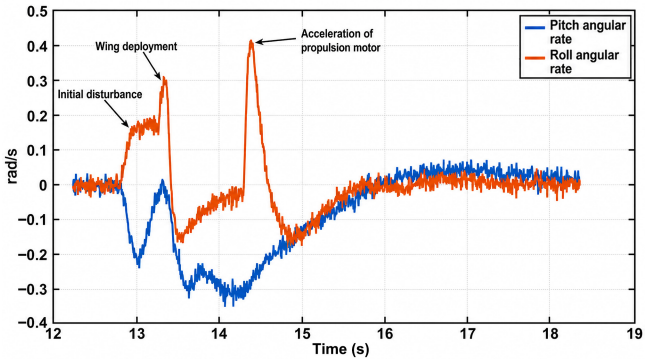



**Fig. 8** Time histories of the roll angular rate without adopting segmental throttle control strategy.

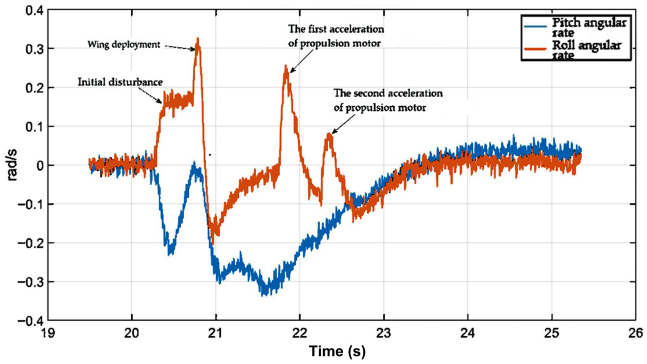



**Fig. 9** Time histories of the roll angular rate adopting the segmental throttle control strategy.

The perturbation ranges in Table 4 are determined from the way the corresponding nominal parameters are obtained, together with worst-case engineering estimates. The inertial parameters are extracted from the three-dimensional Computer-Aided Design (CAD) model in CATIA, and a relatively wide band of ± 30% is adopted to bound the residual error between the CAD-based mass distribution and the as-built vehicle. The control and aerodynamic effectiveness coefficients are computed by CFD, in which the slipstream effect is not considered; a band of ± 20% for the control coefficients and ± 40% for the aerodynamic coefficients is therefore used to cover both the CFD modelling error and the neglected slipstream contribution. The engine thrust is measured by a ground static-thrust test, and a tighter band of ± 10% is assigned in accordance with the repeatability of the measurement and the expected installation losses.

### *Monte Carlo results: statistics of pitch/roll channels*

Latin hypercube sampling[20] is utilized in the Monte Carlo simulations to achieve small-sample convergence. In addition, 100 Monte Carlo tests are shown in Figs 10 and 11.

After completing batches of random sampling simulations, this subsection conducts statistical sorting and quantitative analysis on massive operating data. Key evaluation metrics covering maximum attitude deviation, peak angular rate, actuator saturation frequency, and steady-state tracking error are counted for all sampling cases. The overall distribution range and failure-free proportion of each index are summarized. It can be seen that even with simultaneous deviation of inertia, aerodynamic coefficients, control gains, and thrust within the preset perturbation bounds, the combined scheme of deployment window identification, segmented throttle, and cascaded ADRC still restrains attitude fluctuation within safe allowable limits. The statistical outcomes fully verify that the designed launch control system possesses strong parameter robustness and environmental adaptability.

**Table 4.** Parameter perturbations in Monte Carlo simulations.

| Parameter | Uncertainty (%) |
|---|---|
| Inertial parameters | ± 30 |
| Control coefficients | ± 20 |
| Aerodynamic coefficients | ± 40 |
| Engine thrust | ± 10 |

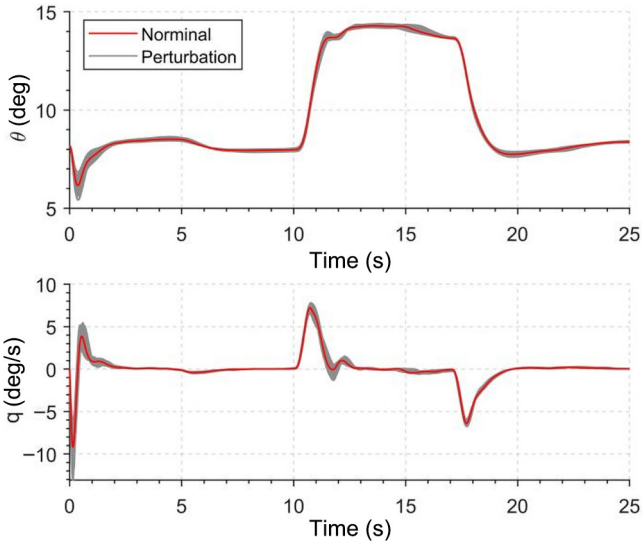



**Fig. 10** Results of Monte Carlo simulations of the ESO-based pitch control.

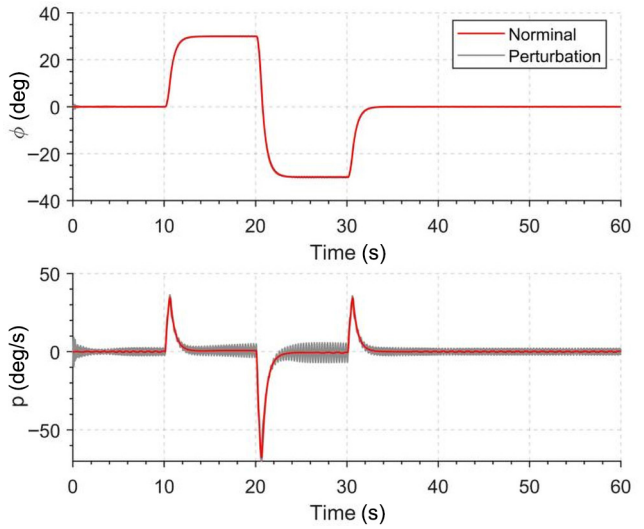



**Fig. 11** Results of Monte Carlo simulations of the ESO-based roll control.

## Criteria for the successful launch process

We conclude four criteria for the successful launch process:

• The pitch angular rate should be limited to ± 0.5 rad/s before the motor is activated.

• After the wings are deployed, the roll angular rate should converge to ± 0.1 rad/s within 0.5 s.

• After the throttle reaches 100%, the roll angular rate should converge to ± 0.05 rad/s within 1.5 s.

• After the throttle reaches 100%, the pitch angular rate should converge to ± 0.05 rad/s within 2 s.

# Discussion

## Tracking performance comparison among multiple control methods

To fully verify the superiority of the proposed cascaded ADRC controller, comparative tests are performed against two typical control strategies, namely conventional PID and nonlinear model predictive control (NMPC). All controllers are configured with the same control bandwidth and actuator constraints. Typical launch disturbances, including wing deployment impact, launcher friction-induced rotation, and motor reverse torque, are applied to the system. To evaluate the performance of the proposed ADRC controller, the following tracking performance index is considered:

$$\mathrm{MSE} = \frac{1}{T}\int_0^T (\theta_c(t) - \theta(t))^2\, dt. \tag{29}$$

In Table 5, we tabulate the performance index for each case. The results show that the proposed ADRC achieves the lowest tracking error.

To ensure a fair comparison, the PID controller is not tuned heuristically: its gains are obtained with the MATLAB PID Tuner, in which the target closed-loop bandwidth is fixed to the same value as that of the proposed ADRC, and the final parameters are then determined by the built-in optimization algorithm to balance tracking accuracy and stability margins. The NMPC controller is likewise configured with the same control bandwidth and actuator constraints.

## Real-world validation

### *Flight test hardware system and test environment conditions*

The flight test was conducted on the gun-launched variable-geometry UAV platform shown in the figure above. The tests were performed in an open outdoor field under normal daytime atmospheric conditions, with light-to-moderate ambient wind. During the trials, the vehicle was subjected to realistic launch disturbances, including launcher-induced rotation at ejection, the impact of wing and tail deployment, and the reaction torque of motor start-up, as well as atmospheric gusts and the run-to-run inconsistency inherent to the launch process. These conditions confirm that the data analyzed below were obtained in a representative real flight environment rather than under idealized settings.

We implemented the flight-control system using a MATLAB/Simulink design flow with Embedded Coder to generate C code for direct deployment. For hardware configuration, the Hardware-in-the-Loop (HIL) simulations were conducted using the autopilot (CPU: STM32F765VGT6,216 MHz) and the simulator (CPU: ARM Cortex-A53, 1.2 GHz). The controllers run at 400 Hz, and the guidance loop runs at 20 Hz.

**Table 5.** Tracking errors of different control methods.

| Method | Value |
|---|---|
| ADRC | 1.5 |
| PID | 3.9 |
| NMPC | 2.4 |

### *Flight data analysis*

Prior to the real-world flight, an extensive series of Monte Carlo simulations was conducted. Throughout the mission scenario, the bandwidth parameters of the extended state observer (ESO) remained fixed, except for $b_q$, which was adjusted according to the Mach number. The attitude tracking performance is illustrated in Figs 12–14. During the mission scenario, both roll and pitch angles were tracked accurately without any steady-state errors or overshoots, demonstrating precise tracking performance.

The actual flight data plotted in Figs 13 and 14 cover the time window of approximately $t$ = 2,650 − 2,950 s, which corresponds to the steady cruise phase after launch rather than the ejection process. These long-duration flight curves are supplemented to further validate the long-term steady-state tracking capability of the cascaded ADRC controller. Apart from anti-disturbance performance during launch and wing deployment, the controller can maintain high-precision stable attitude regulation under continuous steady flight conditions, verifying the full-envelope applicability of the proposed control strategy throughout the whole flight mission.

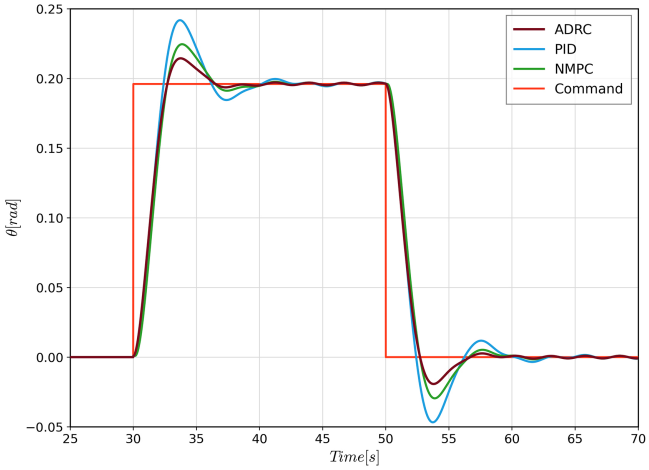



**Fig. 12** The pitch angle tracking performance comparison among ADRC, PID, and NMPC.

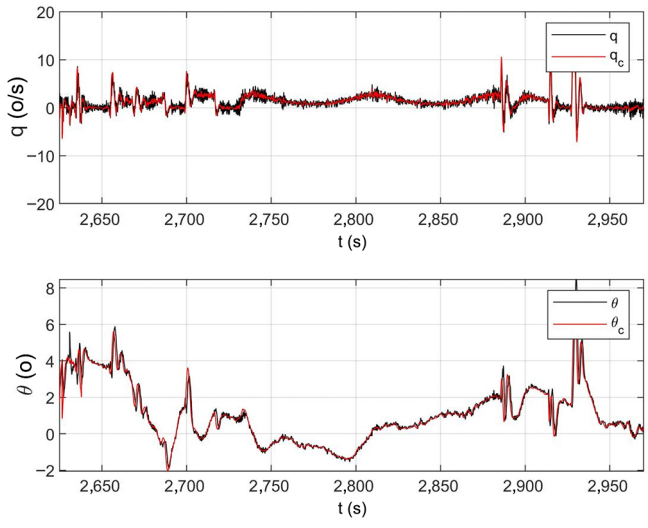



**Fig. 13** Time histories of the pitch channel.

https://doi.org/10.48130/mav-0026-0023

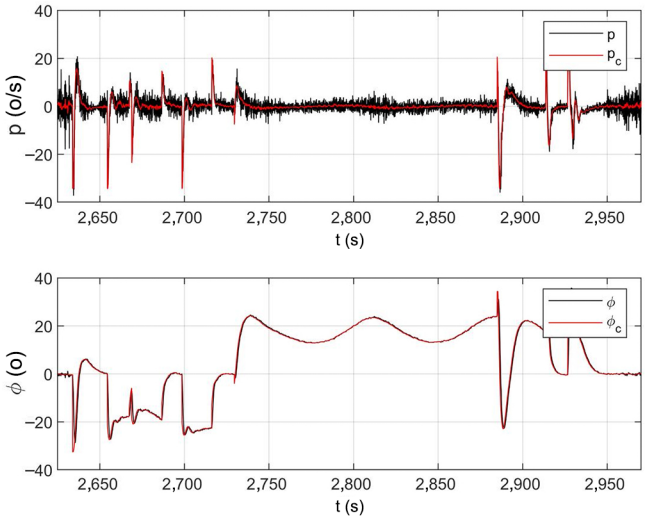



**Fig. 14** Time histories of the roll channel.

## Limitations

Several limitations of the present study should be noted. First, the control design and validation focus on the launch phase and the subsequent cruise condition of a specific gun-launched variable-geometry UAV; the conclusions therefore apply to this configuration and flight envelope, and extension to other vehicles or to the full mission profile would require further verification. In addition, the aerodynamic and control-effectiveness coefficients are obtained from CFD without accounting for the propeller slipstream, and the parameter perturbation bounds are estimated from the data sources and worst-case engineering judgment rather than from a large statistical sample, so the robustness results should be read as representative rather than exhaustive. Finally, the real-world validation is based on a limited number of flight tests covering a steady cruise window rather than a large campaign spanning the complete launch-to-recovery envelope under diverse atmospheric conditions. Addressing these aspects, including slipstream-coupled aerodynamics and more extensive flight testing, constitutes our future work.

# Conclusions

This paper investigated a disturbance rejection control strategy for a variable-geometry, gun-launched UAV. To design a more accurate control law, modal analysis of the aircraft deployment configuration under a nominal mission scenario was first performed. Subsequently, a dedicated control strategy for the launch process was proposed, and a cascaded active disturbance rejection control (ADRC) attitude control system was developed. In addition, a timescale-separation tuning principle was introduced to facilitate the adjustment of the control gains. Monte Carlo simulations and real-world flight validations verified the effectiveness of the proposed launch control strategy and control system. Both simulation and flight results demonstrated improved control stability and robustness: the maximum and mean roll angular rates were reduced by 26% and 33%, respectively, and the maximum and mean pitch angular rates were reduced by 13% and 21%, respectively.

## Author contributions

The authors confirm their contributions to the paper as follows: conceptualization: Wang Z, Xu C; methodology, formal analysis: Wang Z, Liu G; software, writing – original draft preparation: Wang Z; validation, investigation: Wang Z, Liu G, Yi J; resources: Cui C, Liu Y, Xu C; data curation: Wang Z, Cui C; writing – review and editing: Liu G, Cui C, Yi J, Liu Y, Xu C; visualization: Wang Z, Yi J; supervision, funding acquisition: Xu C; project administration: Liu Y, Xu C. All authors reviewed the results and approved the final version of the manuscript.

## Data availability

The flight test data and simulation datasets generated and analyzed during this study are available from the corresponding author upon reasonable request. The data include raw IMU measurements, attitude angles, angular rates, and control surface deflections recorded during the launch phase. Due to the sensitive nature of the UAV platform parameters and proprietary constraints of the collaborative research project, the complete aerodynamic model and embedded control code are not publicly available. Requests for access to the data should be directed to the corresponding author (Chao Xu) and will be evaluated on a case-by-case basis.

## Acknowledgments

This research was funded by the Natural Science Foundation of Zhejiang Province (Grant No. LQK26F030001).

## Conflict of interest

The authors declare that they have no conflict of interest. This research was supported by the Natural Science Foundation of Zhejiang Province. The funding source had no involvement in the study design, data collection, analysis, decision to publish, or preparation of the manuscript. The authors have no financial or personal relationships with other people or organizations that could inappropriately influence or bias this work.

## Dates

Received 2 April 2026; Revised 15 July 2026; Accepted 11 August 2026; Published online 30 October 2026

## References

[1] Torresan C, Berton A, Carotenuto F, Gennaro SFD, Gioli B, et al. 2017. Forestry applications of UAVs in Europe: a review. *International Journal of Remote Sensing* 38(8–10):2427–2447

[2] Fang Z, Savkin AV. 2024. Strategies for optimized UAV surveillance in various tasks and scenarios: a review. *Drones* 8(5):193

[3] MichailidisMG, RutherfordMJ, ValavanisKP. 2020. A survey of controller designs for new generation UAVs: the challenge of uncertain aerodynamic parameters. *International Journal of Control, Automation and Systems* 18(4):801–816

[4] Muchiri GN, Kimathi S. 2022. A review of applications and potential applications of UAV. *Proceedings of 2016 Sustainable Research & Innovation Conference, 4–6 May, 2016*. Nairobi, Kenya: Jomo Kenyatta University of Agriculture and Technology. pp. 280–283 https://sri.jkuat.ac.ke/jkuatsri/index.php/sri/article/view/325

[5] Benyahia ATE, Stanković M, Madonski R, Babayomi O, Manojlović SM. 2025. Improving control performance by cascading observers: case of ADRC with cascade ESO. *IEEE/CAA Journal of Automatica Sinica* 12(8):1702–1712

[6] Gargalakos M. 2024. The role of unmanned aerial vehicles in military communications: application scenarios, current trends, and beyond. *The Journal of Defense Modeling and Simulation: Applications, Methodology, Technology* 21(3):313–321

[7] Løw-Hansen B, Hann R, Gryte K, Johansen TA, Deiler C. 2025. Modeling and identification of a small fixed-wing UAV using estimated aerodynamic angles. *CEAS Aeronautical Journal* 16(2):501–523

[8] Wang Z, Gong Z, Zhang C, He J, Mao S. 2021. Flight test of $L_1$ adaptive control on 120-kg-class electric vertical take-off and landing vehicles. *IEEE Access* 9:163906–163928

[9] Cheng L, Li Y, Yuan J, Ai J, Dong Y. 2023. $L_1$ adaptive control based on dynamic inversion for morphing aircraft. *Aerospace* 10(9):786

[10] Noormohammadi-Asl A, Esrafilian O, Arzati MA, Taghirad HD. 2020. System identification and $H_\infty$-based control of quadrotor attitude. *Mechanical Systems and Signal Processing* 135:106358

[11] Orr JS, Dennehy CJ. 2017. Analysis of the X-15 flight 3-65-97 divergent limit-cycle oscillation. *Journal of Aircraft* 54(1):135–148

[12] Hoffmann C, Werner H. 2015. A survey of linear parameter-varying control applications validated by experiments or high-fidelity simulations. *IEEE Transactions on Control Systems Technology* 23(2):416–433

[13] Zhu E, Pang J, Sun N, Gao H, Sun Q, et al. 2014. Airship horizontal trajectory tracking control based on active disturbance rejection control (ADRC). *Nonlinear Dynamics* 75:725–734

[14] Xia Y, Pu F, Li S, Gao Y. 2016. Lateral path tracking control of autonomous land vehicle based on ADRC and differential flatness. *IEEE Transactions on Industrial Electronics* 63(5):3091–3099

[15] Luo S, Sun Q, Sun M, Tan P, Wu W, et al. 2018. On decoupling trajectory tracking control of unmanned powered parafoil using ADRC-based coupling analysis and dynamic feedforward compensation. *Nonlinear Dynamics* 92:1619–1635

[16] Kong S, Sun J, Qiu C, Wu Z, Yu J. 2021. Extended state observer-based controller with model predictive governor for 3-D trajectory tracking of underactuated underwater vehicles. *IEEE Transactions on Industrial Informatics* 17(9):6114–6124

[17] Gao Z. 2003. Scaling and bandwidth-parameterization based controller tuning. *Proceedings of the American Control Conference, Denver, Colorado, USA, 4–6 June, 2003*. Denver, CO, USA: IEEE pp. 4989–4996 doi: 10.1109/ACC.2003.1242516

[18] Han J. 2009. From PID to active disturbance rejection control. *IEEE Transactions on Industrial Electronics* 56(3):900–906

[19] Dao QT, Dinh VV, Trinh MC, Tran VC, NguyenVL, et al. 2022. Nonlinear extended observer-based ADRC for a lower-limb PAM-based exoskeleton. *Actuators* 11(12):369

[20] Hu X, Chen X, Parks GT, Yao W. 2016. Review of improved Monte Carlo methods in uncertainty-based design optimization for aerospace vehicles. *Progress in Aerospace Sciences* 86:20–27

Copyright: © 2026 by the author(s). Published by Maximum Academic Press, Fayetteville, GA. This article is an open access article distributed under Creative Commons Attribution License (CC BY 4.0), visit https://creativecommons.org/licenses/by/4.0/.